Emergent charge density wave order in the monolayer limit of $1T$-TiTe$_2$ and $1T$-ZrTe$_2$

Jiayuan Zhang, Fei Wang ©, and Chao-Sheng Lian ©*

School of Physics and Microelectronics, Zhengzhou University, Zhengzhou 450001, China

A peculiar charge-density wave (CDW) phase, absent in the bulk, has been widely studied in monolayer $1T$-TiTe$_2$ and newly observed in monolayer $1T$-ZrTe$_2$, while its origin and physical properties remain unclear. Here, we study the distorted lattice and associated energy band renormalization for TiTe$_2$ and ZrTe$_2$ monolayers using first-principles calculations. Both systems are found to exhibit a soft phonon mode at the M point leading to a 2×2 CDW order with similar distortion pattern as in TiSe$_2$ case. Electronic structure results with semilocal functional indicate that the CDW phases of monolayer TiTe$_2$ and ZrTe$_2$ maintain semimetallicity owing to their smaller lattice distortion than in the TiSe$_2$ semiconducting CDW state. The unfolded band structure for monolayer TiTe$_2$ reveals CDW-reconstructed features consistent with experiments, including backfolded bands from Γ to M and vice versa, as well as a stronger energy gapping of the outer valence band along Γ-M due to orbital-dependent p-d hybridization. We also explore the role of exchange interaction in the CDW formation. The nonlocal exchange effect enlarges the lattice distortion amplitude and causes an overcorrection of the electronic structure for monolayer TiTe$_2$, while it barely affects the CDW distortion of monolayer ZrTe$_2$, despite inducing a metal-semiconductor transition. Comparison of the CDW properties of monolayer TiSe$_2$, TiTe$_2$, and ZrTe$_2$ suggests that the judgment of relative CDW strength in these systems should involve coupled electron-lattice modifications. Our work paves the way for elucidating the CDW order in two-dimensional group-IV transition-metal dichalcogenides.

I. INTRODUCTION

Compared with quasi-one-dimensional charge-density wave (CDW) systems where Fermi-surface nesting drives a Peierls instability, layered transition-metal dichalcogenides (TMDs) exhibit more abundant two-dimensional (2D) and three-dimensional (3D) CDW physics, depending on the transition metal's coordination geometry and d-orbital electron count [1–3]. For metallic $2H$-NbSe$_2$ and $2H$-TaSe$_2$, the bulk electronic structure with typical half-filled d bands has no nesting at the CDW wave vector $\mathbf{q}_{\rm CDW}$ [4–7], and momentum-dependent electron-phonon coupling is suggested to drive the CDW order [8–11]. For semimetallic $1T$-TiSe$_2$ with low carrier density, however, the formation mechanism of CDW has been debated among excitonic instability [12–15], Jahn-Teller effect [16–19], electron-phonon coupling [20–22], and electron correlations [23,24]. With rapid advances in synthesis of atomically thin TMDs, dimensionality reduction with varied band structure or screening provides opportunities for both modulating the CDW order and clarifying its physical origin, so as to facilitate the exploitation of the CDW-based electronic devices [25–27].

With declining thickness, charge ordering in TMD films shows diversified evolution trends, such as an enhanced CDW in 2D NbSe$_2$ [28,29] and TiSe$_2$ [30,31] and a nonmonotonic dependence of CDW in 2D VSe$_2$ [32–35]. Among them, the case of $1T$-TiTe$_2$ (TiTe$_2$ in short) is truly surprising because it displays a 2×2 CDW transition only in the monolayer,

but not in the bulk and multilayers [36,37]. This intriguing behavior challenges the general understanding of CDWs in TMDs, still being far from clear due to the distinct thickness dependencies. For monolayer TiTe$_2$, the excitonic or band-type Jahn-Teller interaction is inapplicable given its semimetallic nature with abundant carriers and the absence of a clear conduction-valence band repulsion. Meanwhile, its measured band structure excludes the possibility of any nesting at $\mathbf{q}_{\rm CDW}$ [36], thus pointing to a likely electron-phonon driven picture. A recent experimental work also proposed a band match scenario to explain the different CDW strength in monolayer TiTe$_2$ prepared on graphene and PtTe$_2$ films [38]. In fact, substrate effects such as static-electronic interactions, charge doping, and strain could have significant influence on CDW in the 2D limit. For instance, multilayer and monolayer TiTe$_2$ grown by molecular-beam epitaxy (MBE) on InAs(111)/Si(111) substrates were found to show CDW transitions at room temperature, which were ascribed to the anisotropic strain imposed by the substrate [39]. In addition, a moiré-enhanced CDW was observed for monolayer TiTe$_2$/TiSe$_2$ heterostructures with small turning angles, resulting from the atomic reconstruction and related local strain field [40]. Some theoretical efforts have been devoted to identifying the origin of charge ordering in 2D TiTe$_2$ [41,42]. Guster *et al.* explained its CDW instability with HSE06 functional to treat the exchange interaction, the associated CDW band structure, however, is semiconducting, not in line with the observed metallic one [41]. They also pointed out the possibility of substrate strain-induced CDW in the monolayer, while experiments suggested negligible strain effects [36–38]. Zhou *et al.* claimed that the CDW in TiTe$_2$ is dictated by

*cslian@zzu.edu.cn

the interplay of anharmonicity and exchange enhancement of the electron-phonon interaction, but metallicity of the CDW phase remains unresolved [42]. So far, the mechanism for the CDW formation in monolayer TiTe$_2$ is elusive, and a thorough understanding of its CDW structural and electronic properties is lacking.

Furthermore, its sister compound $1T$-ZrTe$_2$ (ZrTe$_2$ in short) has also generated great interest for studying the effect of dimensionality on CDW. Recent scanning tunneling microscopy or spectroscopy (STM or STS) experiments [43,44] found a similar 2×2 CDW in MBE-grown ZrTe$_2$ films down to the 2D limit. The nonzero dip induced by CDW in the STS spectrum of monolayer ZrTe$_2$ is much deeper than the partial gap feature observed for monolayer TiTe$_2$, raising the issue about their relative CDW strength. Very recently, Song *et al.* performed angle-resolved photoemission spectroscopy (ARPES) studies on the electronic structure of monolayer ZrTe$_2$ and proposed a two-step CDW process, with preformation of the excitonic gas phase at temperatures well above the CDW transition temperature (T_{CDW}), followed by formation of the CDW phase at low temperatures [45]. Currently, there is no consensus on which spectral signal should be used to evaluate the T_{CDW} of group-IV TMDs, which is key to probing the microscopic origin of CDW order. Chen *et al.* extracted $T_{CDW} = 232$ and 92 K for monolayer TiSe$_2$ [30] and TiTe$_2$ [36] using the temperature dependence of the CDW energy gap and the folded valence bands, respectively, while Song *et al.* used the evolution of the 2×2 superlattice peak along with a folded second valence band to extract $T_{CDW} = 130$ K for monolayer ZrTe$_2$ [45]. In this context, a meaningful inquiry is whether a single ordering parameter (lattice or energy band) or their combined changes across the CDW transition can be utilized to determine the CDW strength.

In this work, using first-principles calculations, we elucidate the intrinsic CDW instabilities of 2D TiTe$_2$ and ZrTe$_2$, their distorted lattices, and their modulated electronic properties. Lattice dynamics results show that both monolayer TiTe$_2$ and ZrTe$_2$ have a triple-**q** phonon instability at the M point, and by combining stochastic optimization and a frozen-phonon-like analysis, we confirm the presence of a metallic 2×2 CDW with semilocal functional, in accord with the measured superstructure and STS data. In monolayer TiTe$_2$, including the exchange interaction largely enhances the lattice distortion, but only at an appropriate exchange parameter range can its CDW state maintain the metallic band character. The exchange effect on CDW in monolayer ZrTe$_2$ is marginal, except causing a semiconducting CDW state. By fully examining the distortion amplitude, CDW energy gain, and the renormalized Fermi surface, we unveil the CDW order in monolayer ZrTe$_2$ to be stronger (weaker) than that in monolayer TiTe$_2$ (TiSe$_2$), in good agreement with experiments. We conclude that predicting the strength of a strong-coupling CDW should take into account coupled modifications of the electron-lattice system.

II. COMPUTATIONAL DETAILS

Density-functional theory calculations are carried out within the Vienna *ab initio* simulation package [46,47] using the projector augmented wave method [48,49]. The generalized gradient approximation (GGA) in the scheme of Perdew-Burke-Ernzerhof (PBE) [50] is applied for the exchange-correlation functional. We adopt a plane-wave cutoff energy of 380 eV and a Gaussian smearing with width of 0.03 (0.05) eV for monolayer TiTe$_2$ (ZrTe$_2$). Γ-centered k-point meshes of 24×24×1 and 12×12×1 are used to sample the Brillouin zone (BZ) of the primitive cell and 2×2 supercell, respectively. Lattice parameters and atomic positions are fully relaxed, and the convergence criteria for the energy and force are set to 10^{-8} eV and 10^{-3} eV/Å, respectively. Spin-orbit coupling (SOC) effects are included in the calculation of the electronic band structure and density of states (DOS). The phonon dispersions are calculated using the PHONOPY code [51] based on the finite displacement method, where a 6×6×1 (3×3×1) supercell is applied for the normal (CDW) phase. The Fermi surface is obtained by interpolating the Hamiltonian on the basis of maximally localized Wannier functions using the Wannier90 package [52,53], where the electronic structure around the Fermi level (E_F) is described by 11 Wannier functions (three p states for each Te atom and five d states for the Ti or Zr atom). The HSE functional [54,55] self-consistent calculations with 25% exact exchange are performed on a 12×12×1 k-point mesh for the CDW phase, and the band energy at an arbitrary k point is deduced by Wannier interpolation.

III. NORMAL PHASE

The TiTe$_2$ (ZrTe$_2$) monolayer consists of a transition-metal Ti (Zr) layer sandwiched between two layers of Te with octahedral coordination, crystallizing in a hexagonal Bravais lattice with space group D_{3d}^3 (P3̄m1), as shown in Figs. 1(a) and 1(b). Figure 1(c) presents the phonon dispersions calculated for the 1×1 normal phase of monolayer TiTe$_2$ and ZrTe$_2$ with GGA-PBE functional. In both monolayers, an unstable symmetric triple-**q** soft phonon mode occurs at the M point, pointing to a CDW instability with 2×2 periodicity. These soft modes show close imaginary frequencies, which are roughly half that in monolayer TiSe$_2$ [56,57], implying relatively weak lattice instability in the former two systems. Clearly, our theoretical calculations at the GGA-PBE level have correctly predicted the 2×2 CDW periodicity initially reported for monolayer TiTe$_2$ by Chen *et al.* [36] and for monolayer ZrTe$_2$ by Yang *et al.* [44]. The difference between our phonon results for monolayer TiTe$_2$ and those obtained in prior works [36,41,42] is likely related to the use of different computational methods or parameters such as the electronic smearing (the M-point soft mode becomes unstable only at an enough small smearing, see Figs. S1 and S2 in the Supplemental Material [58]).

The calculated electronic band structures for monolayer TiTe$_2$ and ZrTe$_2$ in the normal state are shown in Figs. 1(d) and 1(e). Both systems behave as a semimetal with three energy bands crossing the E_F, including two valence bands around the Γ point and one conduction band around the M point. The corresponding Fermi surfaces consist of a pair of hole pockets (dominated by Te p orbitals) at Γ and a single elongated elliptical electron pocket (arising from Ti or Zr d orbitals) at M [Figs. 1(f) and 1(g)]. To qualify the band overlap in these semimetals, we define a negative energy
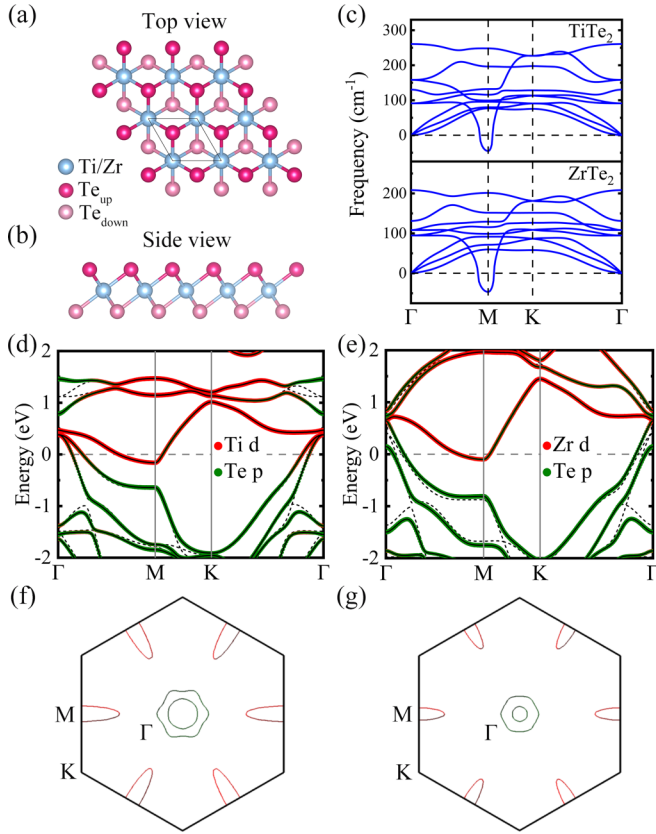
FIG. 1. (a) Top and (b) side views of the TiTe$_2$ and ZrTe$_2$ monolayers. Blue and pink balls denote the Ti or Zr and Te atoms, respectively. (c) Phonon dispersions for monolayer TiTe$_2$ and ZrTe$_2$ in the 1×1 undistorted phase. (d), (e) Electronic band structure for (d) TiTe$_2$ and (e) ZrTe$_2$ monolayer calculated in the normal state with (black solid lines) and without (black dashed lines) SOC, where the orbital character is superimposed on each curve in the former case. The gray dashed line indicates the Fermi level. (f), (g) The corresponding Fermi surfaces under SOC. The Te-derived hole and Ti- and Zr-derived electron pockets are shown in olive and red, respectively.

gap as the difference between the conduction-band minimum at M and the valence-band maximum at Γ, and find that GGA-PBE calculations incorporating the SOC yield an indirect band gap of -0.55 (-0.75) eV in monolayer TiTe$_2$ (ZrTe$_2$, showing a clear SOC-induced splitting of valence bands), in accord with previous calculations on the two systems using the same functional [36,41,59]. Comparing with the theoretical indirect gap of -0.446 eV in the TiSe$_2$ case [57], we see that the conduction-valence band overlap for the TiTe$_2$ or ZrTe$_2$ monolayer is obviously greater, indicating their stronger metallicity. It is also worth noting that the d-derived conduction bandwidth in monolayer ZrTe$_2$ is much larger than the corresponding value in monolayer TiTe$_2$, which suggests more itinerant d-orbital electrons and thus lower correlation in the former.

IV. DISTORTED PHASE

We now turn to investigate the CDW superstructure. We first constructed several randomly distorted 2×2 structures,

which were found to eventually all converge to the same equilibrium configuration after full optimization. Figure 2(a) illustrates the atomic distortion pattern for the relaxed 2×2 superstructure of monolayer TiTe$_2$ (ZrTe$_2$), showing an energy reduction of 0.10 (0.97) meV/f.u. under GGA-PBE relative to the normal phase. In the distorted lattice, one out of four Ti (Zr) atoms (denoted Ti1 or Zr1) in the 2×2 supercell is kept at the same position as in the undistorted $1T$ lattice, forming equal bonds with the top (bottom) Te1 atoms which are displaced clockwise (counterclockwise) in a circular fashion. Thus, Ti1 (Zr1) remains to be the center of the local octahedron generated. By contrast, the other three Ti2 (Zr2) atoms are displaced from the ideal $1T$ lattice positions and move towards the Ti1 (Zr1) atom by the same amplitude δTi/Zr of 0.037 (0.051) Å, generating a four-atom cluster as indicated by the contracted Ti-Ti (Zr-Zr) bonds (olive thick solid lines) in Fig. 2(a). As a result of this movement, Ti2 (Zr2) forms unequal Ti-Te (Zr-Te) bonds with three different lengths, yielding a distorted octahedron with Ti2 (Zr2) off-center. In addition, the three Te1 atoms located over the four-atom Ti/Zr cluster are pushed away from the Ti (Zr) layer, while the remaining Te2 atom gets closer to it. This leads to a slight buckling of Te atomic plane, which we qualify as the height difference between Te1 and Te2, ΔZ_{Te}, as given in Fig. 2(b) along with δTi/Zr.

On top of the stochastic optimization, we further employ the frozen-phonon-like method to study the lattice distortion in the CDW phase. Following the in-plane Ti or Zr displacements suggested by the soft mode (see Table S1 in the Supplemental Material [58]), we set a series of distortion amplitudes δTi/Zr, fully relax the Te atoms for each δTi/Zr, and compute the corresponding total energies. The obtained double-well potential, shown in Figs. 2(c) and 2(d), reflects the local energy landscape of the CDW phase with respect to the Ti/Zr distortion. At low temperature, symmetry-breaking renders the system to freeze in either a configuration with energy minimum at a finite value of δTi/Zr or a degenerate one with a spatial reversal of the distortion. At higher temperature, however, thermal effects allow the system to fluctuate between configurations yielding the high-symmetry 1×1 structure on average. The energy minima for the 2×2 distorted phases of monolayer TiTe$_2$ and ZrTe$_2$ are found to appear at δTi = 0.053 Å and δZr = 0.056 Å, with CDW energy gains of 0.14 and 0.98 meV/f.u., respectively [see the resulting δTi/Zr and ΔZ_{Te} in Fig. 2(b) for comparison with those found by stochastic optimization]. Moreover, the potential-energy surface around the minimum looks very flat for TiTe$_2$ but much deeper for ZrTe$_2$ monolayer. Given this difference, and since local structural relaxation may not produce the most stable structure, it is easy to understand that in TiTe$_2$ the optimized Ti displacement (starting from disordered 2×2 initial structures) is somewhat smaller than that derived from the lowest-energy point of the double-well potential [Fig. 2(b)], while in ZrTe$_2$ the Zr displacement behaves basically the same in both cases. Overall, we can conclude that the transition-metal distortion amplitudes in these two monolayers are comparable to each other, along with a similar Te plane buckling.

It has been known that the inclusion of exchange interaction is essential for the persistence of a robust CDW in
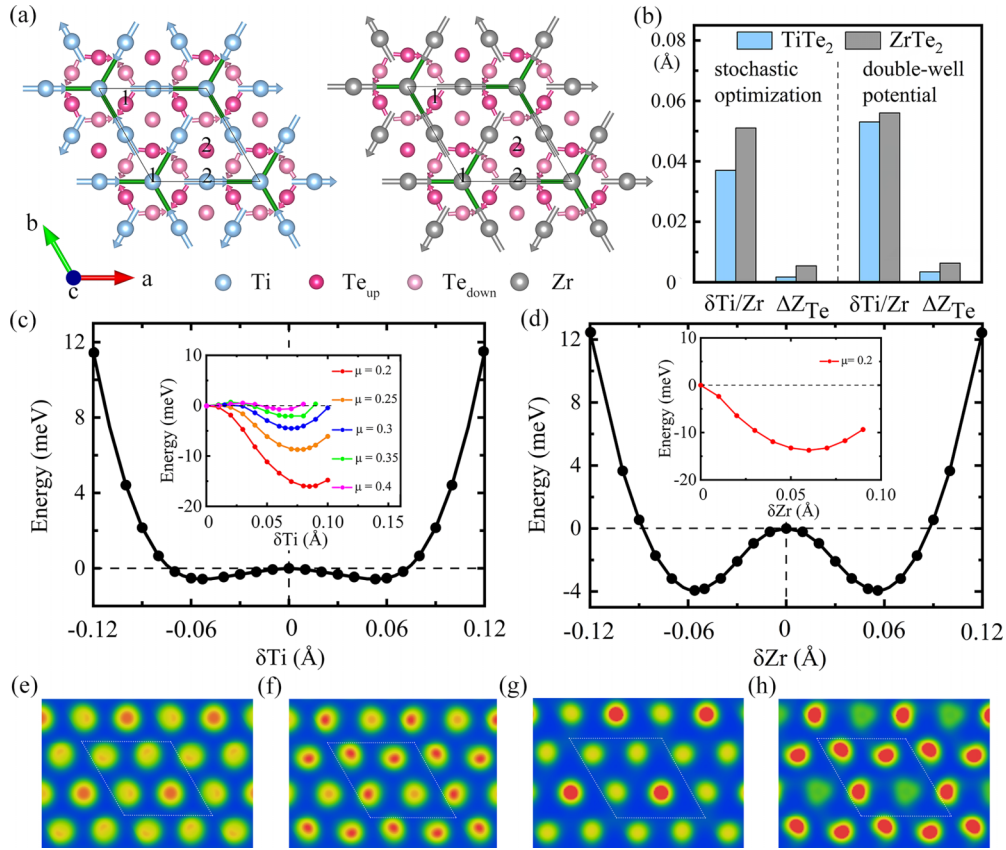
FIG. 2. (a) Atomic distortion pattern in the CDW phase of monolayer $TiTe_2$ and $ZrTe_2$. The length of the arrows is proportional to the magnitude of atomic displacements. Ti1 (Zr1) and Ti2 (Zr2) indicate two nonequivalent Ti (Zr) atoms, while Te1 and Te2 indicate two nonequivalent Te atoms in the top Te layer, with the former located over the four-atom Ti/Zr cluster. (b) Transition-metal distortion $\delta Ti/Zr$ and the height difference between Te1 and Te2 in the CDW phase obtained from the stochastic optimization and the double-well potential. (c), (d) Total energy of the 2×2 superstructure computed under GGA-PBE as a function of δTi or δZr. Insets show the total energy versus distortion curves computed using the HSE functional with different range separation parameter μ. Energies are given relative to the undistorted phase. (e)–(h) Simulated STM patterns for the CDW phase of (e), (f) monolayer $TiTe_2$ and (g), (h) $ZrTe_2$ at $V_{bias} = \pm 50$ mV. The white dashed rhombi indicate the 2×2 superlattice.

monolayer $TiTe_2$ [41,42], but it may overestimate the CDW strength and fail to predict a metallic CDW character as found in ARPES measurements. To conquer this issue, we need to search for an appropriate range of exchange interaction. We have explored the effects of different extents of nonlocal exchange interaction on the $TiTe_2$ CDW phase's stability and band structure by varying the range separation parameter μ used in the HSE functional. The frozen-phonon-like results show that both the Ti distortion amplitude and the CDW energy gain increase with decreasing μ (enhancing the exchange interaction) [see inset of Fig. 2(c) and Fig. S3 in the Supplemental Material [58]]. Meanwhile, μ has a strong influence on the electronic properties: under HSE06 ($\mu = 0.2$), the CDW phase is a semiconductor; with increasing μ (weakening the exchange effect), the corresponding band gap decreases quickly accompanied by the band evolution from a semiconducting to semimetallic character (Fig. S4 in the Supplemental Material [58]). Therefore, only at $0.25 < \mu < 0.4$ can the $TiTe_2$ monolayer hold both the lattice instability and metallicity of the CDW state in accord with experiments [36–38]. For comparison, we also computed the total energy versus distortion curve of monolayer $ZrTe_2$ under HSE06

[inset of Fig. 2(d)] and found the exchange interaction to hardly change its distortion amplitude, which contrasts strongly with the $TiTe_2$ case where the distortion amplitude is very sensitive to the exchange effect. The significant exchange interaction-dependent CDW behavior in monolayer $TiTe_2$ implies more demanding conditions for the CDW formation compared with monolayer $ZrTe_2$ with weaker correlation. Additionally, the GGA+U method had been shown to well describe the normal state's electronic structure of monolayer $TiTe_2$ [36], however, our total-energy calculations here under GGA+U [60] indicate a complete loss of its CDW instability. In fact, the Hubbard U has a negative impact on the CDW order for both monolayer $TiTe_2$ and $ZrTe_2$ (see Fig. S5 in the Supplemental Material [58]).

In the following, for convenience we investigate the CDW properties of monolayer $TiTe_2$ and $ZrTe_2$ by adopting the distorted structures at the minima of double-well potentials under GGA-PBE, which show reasonable agreement with experiments except where explicitly stated otherwise. To verify the distorted CDW phases predicted here, we have simulated their STM patterns under both positive and negative bias, corresponding to the spatial distributions of empty and
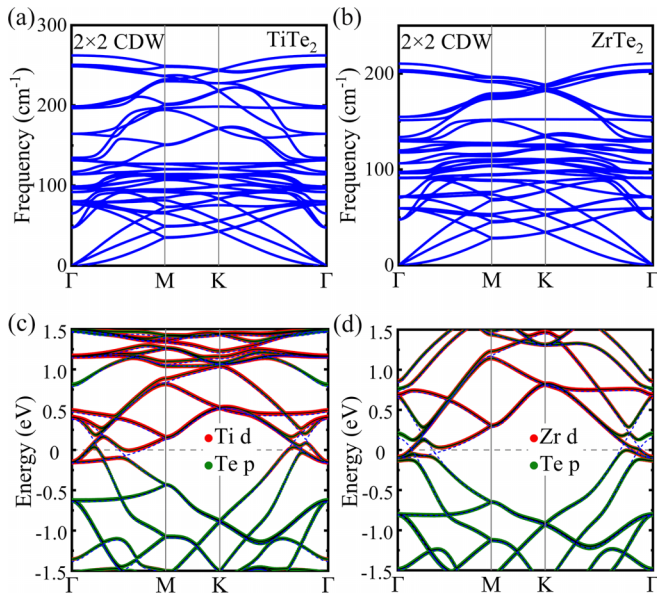
FIG. 3. (a), (b) Phonon dispersions of the distorted CDW phase for monolayer $TiTe_2$ and $ZrTe_2$ in the 2×2 supercell BZ. (c), (d) Electronic band structure of the distorted CDW phase (black solid lines) in comparison with that of the corresponding 2×2 normal phase (blue dashed lines).

occupied states, respectively. The topographic images obtained at 50 and -50 mV for monolayer $TiTe_2$ [Figs. 2(e) and 2(f)] and $ZrTe_2$ [Figs. 2(g) and 2(h)] indicate that the spatial intensity of the CDW modulation reverses between two polarities. This reveals a contrast inversion serving as a signature of CDW. The detailed STM pattern is further found to be closely related to the out-of-plane Te displacements. Under negative bias [Figs. 2(f) and 2(h)], the highest three Te atoms kept away from the four-atom Ti or Zr cluster give rise to three largest bright spots, while the remaining lower Te atom located closer to the Ti or Zr layer generates one dim spot. From the energy band point of view, the "three bright–one dim" pattern at negative bias is associated with electronic states in the filled valence bands characteristic of Te p orbitals, thus reflecting the different heights of the two nonequivalent Te atoms. Notice that, despite the absence of a high-resolution CDW STM image, our simulated STM patterns for the $TiTe_2$ and $ZrTe_2$ monolayers are in line with the STM images observed in $TiSe_2$ CDW phase [61,62], suggesting a common CDW distortion in group-IV TMDs.

Next we examine the phonon dispersions and electronic band structure of the distorted CDW phase. For both monolayer $TiTe_2$ and $ZrTe_2$, the absence of any imaginary phonon frequencies in the whole 2×2 supercell BZ [Figs. 3(a) and 3(b)] demonstrates the dynamical stability of the distorted configuration at the potential-energy minimum deemed as the ground-state CDW structure. The GGA-PBE band-structure results [Figs. 3(c) and 3(d)] show that there still remain some energy bands crossing the E_F, pointing to a metallic CDW state. The folded conduction and valence bands touch near the zone center of the supercell BZ and, due to the CDW distortion, multiple partial gaps form around the crossing points (present in the 2×2 normal phase), which lower

(increase) the energy of the filled (empty) states near E_F. This feature is in contrast to the full band gap occurring in the CDW phase of monolayer $TiSe_2$ [30,57]. Comparing the transition-metal distortion (0.09 Å) in the $TiSe_2$ case with that in the $TiTe_2$ or $ZrTe_2$ case (0.053 or 0.056 Å, respectively) in Table I and considering their distinct CDW band features (semiconducting versus metallic), we conclude that the electronic structure in the CDW state of group-IV TMDs strongly depends on the magnitude of the distortion of transition-metal atoms, and their CDW formation proves to be of strong electron-phonon coupling origin [2]. Note that our theoretical CDW band structure for monolayer $TiTe_2$ is similar to that reported for the same system under 2% tensile strain by Guster *et al.* [41]. This is understandable because the Ti distortion (0.053 Å) obtained here in the absence of strain is close to 0.057 Å obtained in that work under strain, which further supports our above point. Summing up, the CDW ground state for the $TiTe_2$ or $ZrTe_2$ monolayer hosts metallicity owing to a relatively small CDW distortion amplitude.

To clarify in detail the modulation of electronic properties by CDW and facilitate direct comparison with experimental spectral measurements, we unfold the band structure of the 2×2 CDW phase to the original 1×1 BZ [63] and show the results for monolayer $TiTe_2$ and $ZrTe_2$ in Figs. 4(a)–4(c) and 4(g)–4(i), respectively. Clearly, both systems exhibit obvious band spectral weight transfer across the BZ and energy gapping around the E_F. The two valence bands are backfolded from Γ to M, accompanied by a concomitant backfolding of the conduction band from M to Γ, and the backfolded signal at M (Γ) is significantly smaller than the spectral weight of the main band at Γ (M). In particular, the closeups of Fig. 4(a) for monolayer $TiTe_2$ [Figs. 4(b) and 4(c)] are consistent with the measured ARPES spectrum [36–38], noticing that the slopes of two backfolded valence bands around M would be better replicated by using the HSE functional [42]. Interestingly, for the outer main valence band around Γ [Fig. 4(c)], a considerably large energy gap appears near E_F (olive circle) along the Γ-M direction, while the energy gap for the inner valence band is very small (blue circle) [see similar behavior for monolayer $ZrTe_2$ in Fig. 4(i)]. The opening of such momentum-dependent gaps implies orbital-dependent hybridization between the folded conduction and valence bands in the CDW state [37].

Below we focus on monolayer $TiTe_2$ to discuss the band hybridization around Γ across the CDW transition. As seen from the normal state's band structure in Fig. 4(e), along Γ-M, the orbital character is predominantly of Te p_x for the outer and of Te p_y for the inner valence band. Meanwhile, one out of three backfolded conduction bands shows mainly $d_{x'y'}$ character in the local octahedral basis [64,65] [$x'y'z'$ in Fig. 4(d)], and given the threefold rotational symmetry of the system, we just need to consider its overlap with the p states for simplicity. Two key symmetries of the ideal $1T$ crystal structure can be found from Fig. 4(d): a mirror plane m that is oriented along the vertical (y) direction of the global coordinate system, and a C_2 rotational symmetry axis oriented along the horizontal (x) direction. The band made from the $d_{x'y'}$ orbital on Ti has even parity under both symmetries. The p_x-derived band, however, is even under C_2 and odd

TABLE I. Comparison of the lattice constant a (Å), the Fermi-level DOS of the normal (CDW) phase N_F^{nor} (N_F^{CDW}) (states eV^{-1} f.u.$^{-1}$), the transition-metal distortion δTi/Zr (Å), and the CDW energy gain $|\Delta E|$ (meV/f.u.) between monolayer TiSe$_2$, TiTe$_2$, and ZrTe$_2$. The measured values of T_{CDW} (K) for the three systems are also listed.

System	1×1 normal		2×2 CDW			
	a	N_F^{nor}	δTi/Zr	$|\Delta E|$	N_F^{CDW}	T_{CDW}
TiSe$_2$	3.54	1.22	0.090	4.62	0	232 ± 5 [30]
TiTe$_2$	3.75	1.61	0.053	0.14	1.41	92 ± 5 [36]
ZrTe$_2$	3.97	1.14	0.056	0.98	0.63	130 ± 20 [45]

under m, and the opposite is true for the p_y-derived band. Thus, in the 2×2 normal state, the overlap integrals $\langle p_x | d_{x'y'} \rangle$ and $\langle p_y | d_{x'y'} \rangle$ are basically zero, and no gap is expected to open at the crossing of the p-d bands. Upon the CDW transition, phonon mode softening leads to a periodic lattice distortion [Fig. 4(d)] that breaks the mirror symmetry. The hybridization between p_x- and d-derived states is then allowed due to the lacking of enforced constraints from mirror symmetry, while with C_2 symmetry, the hybridization of the p_y- and d-derived states remains forbidden. Consequently, the outer p_x-derived valence band undergoes a marked energy gapping below E_F due to the selective p-d hybridization, leaving the inner p_y-derived one nearly unaffected. In our work, such a strong symmetry constraint is weakened by the inclusion of SOC, which slightly mixes the Te p_x and p_y states. Hence, a tiny gap also opens in the inner valence band. We emphasize that

although the above arguments are formally valid only at Γ preserving both the C_2 and m symmetries, they establish the basis for exploring the band hybridization throughout the BZ. In addition, compared with TiTe$_2$ case, the inner valence band around Γ for monolayer ZrTe$_2$ exhibits more sizable energy gapping near E_F, which can be ascribed to a larger mixing of Te p_x and p_y states under SOC [Fig. 4(k)].

Furthermore, we examine the CDW strength for the TiTe$_2$ or ZrTe$_2$ monolayer via the CDW-renormalized electronic DOS, shown in Figs. 4(f) and 4(l). It is seen that the major peak positions of the DOS in the TiTe$_2$ CDW phase change little with respect to the normal phase [Fig. 4(f)], and agree well with the low-temperature STS data taken over a wide energy range by Chen *et al.* [36]. Moreover, its DOS displays a shallow dip around E_F, indicating a slight decrease in the number of electronic states on the Fermi surface. In contrast, the DOS in the ZrTe$_2$ CDW phase shows a much
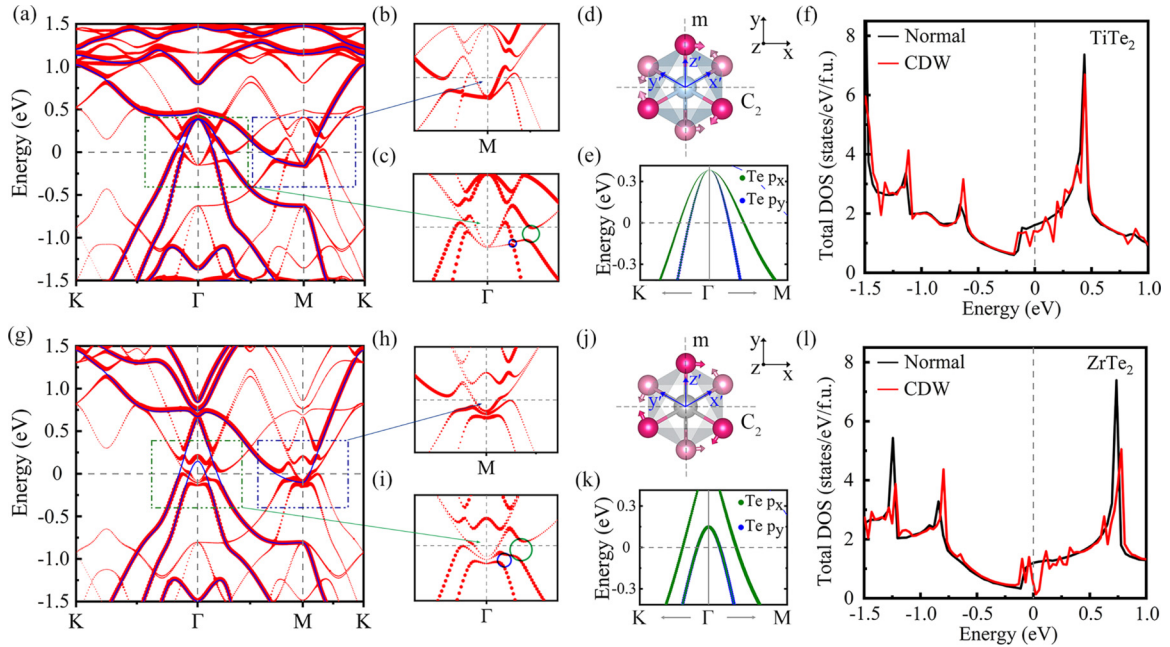

FIG. 4. Unfolded band structure in the 1×1 BZ for the CDW phase of (a) monolayer TiTe$_2$ and (g) ZrTe$_2$ (red dots indicating the spectral weights) compared with the band structure of the 1×1 normal phase (blue solid lines). The closeups of the areas near M and Γ highlighted by dashed rectangles are presented in panels (b) and (c) for TiTe$_2$ and in panels (h) and (i) for the ZrTe$_2$ monolayer. Olive and blue circles in panels (c) and (i) indicate the energy gaps opened on the outer and inner valence bands along Γ-M, being 0.09 and 0.017 eV for the TiTe$_2$ monolayer and 0.12 and 0.046 eV for the ZrTe$_2$ monolayer, respectively. (d), (j) The ideal 1T lattice showing both a mirror symmetry m and a C_2 rotational symmetry, where $x'y'z'$ defines a local octahedral basis. The arrows depict the movement of Te atoms in the CDW state. (e), (k) The normal phase's valence bands around Γ weighted by Te p_x and p_y orbitals. (f), (l) Electronic DOS of the CDW phase in comparison with that of the normal phase.
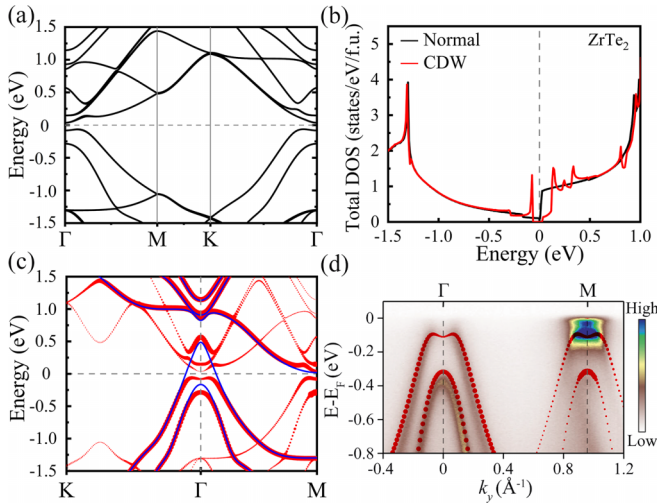
FIG. 5. (a), (b) Electronic band structure and DOS of monolayer $ZrTe_2$ calculated in the CDW state using the HSE06 functional with SOC. (c) Unfolded band structure in the 1×1 BZ (red dots), compared with the normal phase's HSE06 band structure (blue solid lines). (d) Comparison of the theoretical result with the ARPES spectrum measured along Γ-M [45] (taken from Ref. [45], Copyright ©2023 Springer Nature). The Fermi energy in the former is artificially shifted upward by 0.03 eV to mimic electron doping.

deeper and wider dip, with a more substantial reduction of electronic states near E_F [Fig. 4(1)]. This difference stems from the strikingly different Fermi-surface energy gapping extents in the two systems as corroborated by our band unfolding results in Figs. 4(a) and 4(g) (see Fig. S6 for a more detailed analysis in the Supplemental Material [58]). Notice that, for both monolayer $TiTe_2$ and $ZrTe_2$, the dip feature in the theoretically calculated DOS of the distorted phase coincides with the "quasienergy-gap" observed for the CDW state in the experimental STS spectrum [36,44]. Importantly, the more significant modification of DOS in $ZrTe_2$ case points to its intrinsically stronger CDW order. This is in line with our total-energy result that monolayer $ZrTe_2$ has a much larger CDW energy gain than monolayer $TiTe_2$, although not intimately linked to their actually very close transition metal distortion amplitudes (see Table I). As such, the relative CDW strength in these TMDs cannot be determined by a single parameter alone but relies on composite factors as the modulated lattice, modified electronic DOS, and the CDW energy gain, which consolidates their strong-coupling CDW nature.

Based on the above discussions, we have predicted both the CDW phases of monolayer $TiTe_2$ and $ZrTe_2$ to be semimetallic within the GGA-PBE framework, agreeing with most of the previous works [36–40,44]. However, a recent ARPES work by Song et al. [45] revealed monolayer $ZrTe_2$ behaves as a semiconductor in the CDW state. To further explore the electronic properties of monolayer $ZrTe_2$ across the CDW transition, we calculate its band structure and DOS in both the normal and CDW states using the HSE06 functional. As shown in Figs. 5(a) and 5(b), a clear full gap occurs between the conduction and valence bands of the CDW phase across the BZ, in contrast with the aforementioned GGA-PBE

result. Figure 5(c) presents the corresponding unfolded band structure in the 1×1 BZ, along with the normal phase's HSE06 band structure. Compared with semilocal functional case [Fig. 4(g)], in the normal phase the overlap between the conduction and valence bands is reduced upon introducing the exchange interaction [Fig. 5(c)], and both its two valence bands move downwards, with the second one sinking below the E_F. The first valence band still crosses the Fermi surface, but after the CDW transition, it is severely gapped yielding a nearly flat band below E_F. Therefore, a semiconducting CDW state develops due to the combined effects of exchange interaction and CDW energy gapping. As can be seen from Fig. 5(d), our HSE06 calculations replicate the experimentally observed two backfolded valence bands [45] relatively well, if considering a 0.03 eV upward shift of the Fermi energy to mimic possible electron doping from the substrate [43,44]. Overall, for monolayer $ZrTe_2$, the conduction-valence band overlap is overestimated under GGA-PBE functional and thus, in spite of a strong Fermi-surface energy gapping by CDW, it maintains semimetallicity; only by treating the exchange effect, can the CDW phase further experience a semimetal-semiconductor transition.

V. CONCLUSIONS

In summary, we have conducted comprehensive first-principles studies on the CDW instability, associated lattice distortion, and renormalization of the electronic structure in both monolayer $TiTe_2$ and $ZrTe_2$. The calculated phonon dispersions showing an M-point soft mode verify the emergent 2×2 CDW order in the $TiTe_2$ or $ZrTe_2$ monolayer, whose distortion pattern is found to feature a common four-atom Ti or Zr cluster. The GGA-PBE electronic structure results reveal their semimetallic CDW character as opposed to the $TiSe_2$ case, in accord with STS spectra observed on the two systems [36,44]. For monolayer $TiTe_2$, the unfolded band structure of the CDW phase unveils the backfolded valence (conduction) band spectral weights around M (Γ) and a momentum-dependent energy gapping of the main valence bands arising from the orbital-dependent p-d hybridization, consistent with ARPES experiments [36–38]. Further HSE functional calculations show that the nonlocal exchange interaction induces significant corrections to the CDW distortion and electronic properties of monolayer $TiTe_2$, and only with an appropriate range separation exchange parameter can it hold a metallic CDW state. In addition, for monolayer $ZrTe_2$, the exchange interaction has a weak impact on its lattice distortion amplitude, but is key to forming a semiconducting CDW state.

We have also elucidated the strength sequence of CDWs in monolayer $TiSe_2$, $TiTe_2$, and $ZrTe_2$. The transition-metal distortion amplitudes in the CDW phases of monolayer $TiTe_2$ and $ZrTe_2$ are notably smaller than that of monolayer $TiSe_2$, which suggests that the CDW order is most robust in the latter diselenide. Meanwhile, these amplitudes are nearly of the same size, implying comparably weaker CDW orders in the two ditellurides. The greater CDW energy gain and Fermi-surface gapping in monolayer $ZrTe_2$ than in monolayer $TiTe_2$ further confirm that the CDW strength in the former surpasses that in the latter. Such a strength sequence of CDWs in these

three monolayers is well supported by the experimentally reported CDW transition temperatures ($T_{CDW} = 232$, 130, and 92 K for monolayer $TiSe_2$, $ZrTe_2$, and $TiTe_2$, respectively) [30,36,45]. We thus conclude that identifying the relative CDW strength in different systems need to analyze in detail ordering parameters concerning both the lattice distortion and the modulation of electronic energy bands, which constitute crucial ingredients in determining the transition temperature of a strong-coupling CDW. The present work provides a basis for better understanding the strength, physical properties as well as the origin of CDWs in group-IV TMDs in the 2D limit.

[1] J. A. Wilson, F. J. Di Salvo, and S. Mahajan, Charge-density waves and superlattices in the metallic layered transition metal dichalcogenides, Adv. Phys. **24**, 117 (1975).

[2] K. Rossnagel, On the origin of charge-density waves in select layered transition-metal dichalcogenides, J. Phys.: Condens. Matter **23**, 213001 (2011).

[3] H. Yang, S. W. Kim, M. Chhowalla, and Y. H. Lee, Structural and quantum-state phase transitions in van der Waals layered materials, Nat. Phys. **13**, 931 (2017).

[4] M. D. Johannes and I. I. Mazin, Fermi surface nesting and the origin of charge density waves in metals, Phys. Rev. B **77**, 165135 (2008).

[5] T. Yokoya, T. Kiss, A. Chainani, S. Shin, M. Nohara, and H. Takagi, Fermi surface sheet-dependent superconductivity in $2H$-$NbSe_2$, Science **294**, 2518 (2001).

[6] Y. W. Li, J. Jiang, H. F. Yang, D. Prabhakaran, Z. K. Liu, L. X. Yang, and Y. L. Chen, Folded superstructure and degeneracy-enhanced band gap in the weak-coupling charge density wave system $2H$-$TaSe_2$, Phys. Rev. B **97**, 115118 (2018).

[7] C. J. Arguello, E. P. Rosenthal, E. F. Andrade, W. Jin, P. C. Yeh, N. Zaki, S. Jia, R. J. Cava, R. M. Fernandes, A. J. Millis, T. Valla, R. M. Osgood, Jr., and A. N. Pasupathy, Quasiparticle interference, quasiparticle interactions, and the origin of the charge density wave in $2H$-$NbSe_2$, Phys. Rev. Lett. **114**, 037001 (2015).

[8] F. Weber, S. Rosenkranz, J.-P. Castellan, R. Osborn, R. Hott, R. Heid, K.-P. Bohnen, T. Egami, A. H. Said, and D. Reznik, Extended phonon collapse and the origin of the charge-density wave in $2H$-$NbSe_2$, Phys. Rev. Lett. **107**, 107403 (2011).

[9] M. Calandra, I. I. Mazin, and F. Mauri, Effect of dimensionality on the charge-density wave in few-layer $2H$-$NbSe_2$, Phys. Rev. B **80**, 241108(R) (2009).

[10] Y. Ge and A. Y. Liu, Effect of dimensionality and spin-orbit coupling on charge-density-wave transition in $2H$-$TaSe_2$, Phys. Rev. B **86**, 104101 (2012).

[11] C.-S. Lian, C. Heil, X. Liu, C. Si, F. Giustino, and W. Duan, Coexistence of superconductivity with enhanced charge density wave order in the two-dimensional limit of $TaSe_2$, J. Phys. Chem. Lett. **10**, 4076 (2019).

[12] H. Cercellier, C. Monney, F. Clerc, C. Battaglia, L. Despont, M. G. Garnier, H. Beck, P. Aebi, L. Patthey, H. Berger, and L. Forró, Evidence for an excitonic insulator phase in $1T$-$TiSe_2$, Phys. Rev. Lett. **99**, 146403 (2007).

[13] C. Monney, C. Battaglia, H. Cercellier, P. Aebi, and H. Beck, Exciton condensation driving the periodic lattice distortion of $1T$-$TiSe_2$, Phys. Rev. Lett. **106**, 106404 (2011).

[14] M. Cazzaniga, H. Cercellier, M. Holzmann, C. Monney, P. Aebi, G. Onida, and V. Olevano, Ab initio many-body effects in $TiSe_2$: A possible excitonic insulator scenario from GW band-shape renormalization, Phys. Rev. B **85**, 195111 (2012).

[15] A. Kogar, M. S. Rak, S. Vig, A. A. Husain, F. Flicker, Y. I. Joe, L. Venema, G. J. MacDougall, T. C. Chiang, E. Fradkin, J. van Wezel, and P. Abbamonte, Signatures of exciton condensation in a transition metal dichalcogenide, Science **358**, 1314 (2017).

[16] A. Wegner, J. Zhao, J. Li, J. Yang, A. A. Anikin, G. Karapetrov, K. Esfarjani, D. Louca, and U. Chatterjee, Evidence for pseudo-Jahn-Teller distortions in the charge density wave phase of $1T$-$TiSe_2$, Phys. Rev. B **101**, 195145 (2020).

[17] K. Rossnagel, L. Kipp, and M. Skibowski, Charge-density-wave phase transition in $1T$-$TiSe_2$: Excitonic insulator versus band-type Jahn-Teller mechanism, Phys. Rev. B **65**, 235101 (2002).

[18] H. P. Hughes, Structural distortion in $TiSe_2$ and related materials: A possible Jahn-Teller effect? J. Phys. C: Solid State Phys. **10**, L319 (1977).

[19] M. H. Whangbo and E. Canadell, Analogies between the concepts of molecular chemistry and solid-state physics concerning structural instabilities. Electronic origin of the structural modulations in layered transition metal dichalcogenides, J. Am. Chem. Soc. **114**, 9587 (1992).

[20] F. Weber, S. Rosenkranz, J.-P. Castellan, R. Osborn, G. Karapetrov, R. Hott, R. Heid, K.-P. Bohnen, and A. Alatas, Electron-phonon coupling and the soft phonon mode in $TiSe_2$, Phys. Rev. Lett. **107**, 266401 (2011).

[21] M. Hellgren, J. Baima, R. Bianco, M. Calandra, F. Mauri, and L. Wirtz, Critical role of the exchange interaction for the electronic structure and charge-density-wave formation in $TiSe_2$, Phys. Rev. Lett. **119**, 176401 (2017).

[22] M. Calandra and F. Mauri, Charge-density wave and superconducting dome in $TiSe_2$ from electron-phonon interaction, Phys. Rev. Lett. **106**, 196406 (2011).

[23] D. Novko, Z. Torbatian, and I. Lončarić, Electron correlations rule the phonon-driven instability in single-layer $TiSe_2$, Phys. Rev. B **106**, 245108 (2022).

[24] Z. Zhu, Y. Cheng, and U. Schwingenschlögl, Origin of the charge density wave in $1T$-$TiSe_2$, Phys. Rev. B **85**, 245133 (2012).

[25] K. Lasek, J. Li, S. Kolekar, P. M. Coelho, L. Guo, M. Zhang, Z. Wang, and M. Batzill, Synthesis and characterization of 2D transition metal dichalcogenides: Recent progress from a vacuum surface science perspective, Surf. Sci. Rep. **76**, 100523 (2021).

[26] C.-S. Lian, Interplay of charge ordering and superconductivity in two-dimensional $2H$ group V transition-metal dichalcogenides, Phys. Rev. B **107**, 045431 (2023).

[27] Z. Xu, H. Yang, X. Song, Y. Chen, H. Yang, M. Liu, Z. Huang, Q. Zhang, J. Sun, L. Liu, and Y. Wang, Topical review: Recent progress of charge density waves in 2D transition metal dichalcogenide-based heterojunctions and their applications, Nanotechnol. **32**, 492001 (2021).

[28] X. Xi, L. Zhao, Z. Wang, H. Berger, L. Forró, J. Shan, and K. F. Mak, Strongly enhanced charge-density-wave order in monolayer $NbSe_2$, Nat. Nanotechnol. **10**, 765 (2015).

[29] C.-S. Lian, C. Si, and W. Duan, Unveiling charge-density wave, superconductivity, and their competitive nature in two-dimensional $NbSe_2$, Nano Lett. **18**, 2924 (2018)

[30] P. Chen, Y.-H. Chan, X.-Y. Fang, Y. Zhang, M. Y. Chou, S.-K. Mo, Z. Hussain, A.-V. Fedorov, and T.-C. Chiang, Charge density wave transition in single-layer titanium diselenide, Nat. Commun. **6**, 8943 (2015).

[31] X.-Y. Fang, H. Hong, P. Chen, and T.-C. Chiang, X-ray study of the charge-density-wave transition in single-layer $TiSe_2$, Phys. Rev. B **95**, 201409(R) (2017).

[32] Á. Pásztor, A. Scarfato, C. Barreteau, E. Giannini, and C. Renner, Dimensional crossover of the charge density wave transition in thin exfoliated VSe_2, 2D Mater. **4**, 041005 (2017).

[33] P. Chen, Y.-H. Chan, R.-Y. Liu, H. T. Zhang, Q. Gao, A.-V. Fedorov, M. Y. Chou, and T.-C. Chiang, Dimensional crossover and symmetry transformation of charge density waves in VSe_2, Phys. Rev. B **105**, L161404 (2022).

[34] P. Chen, W. W. Pai, Y.-H. Chan, V. Madhavan, M. Y. Chou, S.-K. Mo, A.-V. Fedorov, and T.-C. Chiang, Unique gap structure and symmetry of the charge density wave in single-layer VSe_2, Phys. Rev. Lett. **121**, 196402 (2018).

[35] A. O. Fumega, J. Diego, V. Pardo, S. Blanco-Canosa, and I. Errea, Anharmonicity reveals the tunability of the charge density wave orders in monolayer VSe_2, Nano Lett. **23**, 1794 (2023).

[36] P. Chen, W. W. Pai, Y.-H. Chan, A. Takayama, C.-Z. Xu, A. Karn, S. Hasegawa, M.-Y. Chou, S.-K. Mo, A.-V. Fedorov, and T.-C. Chiang, Emergence of charge density waves and a pseudogap in single-layer $TiTe_2$, Nat. Commun. **8**, 516 (2017).

[37] T. Antonelli, W. Rahim, M. D. Watson, A. Rajan, O. J. Clark, A. Danilenko, K. Underwood, I. Marković, E. Abarca-Morales, S. R. Kavanagh *et al.*, Orbital-selective band hybridisation at the charge density wave transition in monolayer $TiTe_2$, npj Quantum Mater. **7**, 98 (2022).

[38] M.-K. Lin, J. A. Hlevyack, P. Chen, R.-Y. Liu, S.-K. Mo, and T.-C. Chiang, Charge instability in single-Layer $TiTe_2$ mediated by van der Waals bonding to substrates, Phys. Rev. Lett. **125**, 176405 (2020).

[39] S. Fragkos, R. Sant, C. Alvarez, A. Bosak, P. Tsipas, D. Tsoutsou, H. Okuno, G. Renaud, and A. Dimoulas, Room temperature commensurate charge density wave in epitaxial strained $TiTe_2$ multilayer films, Adv. Mater. Interfaces **6**, 1801850 (2019).

[40] W.-M. Zhao, L. Zhu, Z. Nie, Q.-Y. Li, Q.-W. Wang, L.-G. Dou, J.-G. Hu, L. Xian, S. Meng, and S.-C. Li, Moiré enhanced charge density wave state in twisted $1T$-$TiTe_2$/$1T$-$TiSe_2$ heterostructures, Nat. Mater. **21**, 284 (2022).

[41] B. Guster, R. Robles, M. Pruneda, E. Canadell, and P. Ordejón, 2×2 charge density wave in single-layer $TiTe_2$, 2D Mater. **6**, 015027 (2019).

[42] J. Sky Zhou, R. Bianco, L. Monacelli, I. Errea, F. Mauri, and M. Calandra, Theory of the thickness dependence of the charge

[43] M.-Q. Ren, S. Han, J.-Q. Fan, L. Wang, P. Wang, W. Ren, K. Peng, S. Li, S.-Z. Wang, F.-W. Zheng *et al.*, Semiconductor-metal phase transition and emergent charge density waves in $1T$-ZrX_2 (X = Se, Te) at the two-dimensional limit, Nano Lett. **22**, 476 (2022).

[44] L.-N. Yang, Y.-J. Xu, Q.-Y. Li, Y.-X. Meng, Y.-F. Zhao, and S.-C. Li, Coexistence of the charge density wave state and linearly dispersed energy band in $1T$-$ZrTe_2$ monolayer, Appl. Phys. Lett. **120**, 073105 (2022).

[45] Y. Song, C. Jia, H. Xiong, B. Wang, Z. Jiang, K. Huang, J. Hwang, Z. Li, C. Hwang, Z. Liu *et al.*, Signatures of the exciton gas phase and its condensation in monolayer $1T$-$ZrTe_2$, Nat. Commun. **14**, 1116 (2023).

[46] G. Kresse and J. Furthmüller, Efficient iterative schemes for *ab initio* total-energy calculations using a plane-wave basis set, Phys. Rev. B **54**, 11169 (1996).

[47] G. Kresse and J. Furthmüller, Efficiency of *ab-initio* total energy calculations for metals and semiconductors using a plane-wave basis set, Comput. Mater. Sci. **6**, 15 (1996).

[48] P. E. Blöchl, Projector augmented-wave method, Phys. Rev. B **50**, 17953 (1994).

[49] G. Kresse and D. Joubert, From ultrasoft pseudopotentials to the projector augmented-wave method, Phys. Rev. B **59**, 1758 (1999).

[50] J. P. Perdew, K. Burke, and M. Ernzerhof, Generalized gradient approximation made simple, Phys. Rev. Lett. **77**, 3865 (1996).

[51] A. Togo, F. Oba, and I. Tanaka, First-principles calculations of the ferroelastic transition between rutile-type and $CaCl_2$-type SiO_2 at high pressures, Phys. Rev. B **78**, 134106 (2008).

[52] N. Marzari, A. A. Mostofi, J. R. Yates, I. Souza, and D. Vanderbilt, Maximally localized Wannier functions: Theory and applications, Rev. Mod. Phys. **84**, 1419 (2012).

[53] G. Pizzi, V. Vitale, R. Arita, S. Bluegel, F. Freimuth, G. Géranton, M. Gibertini, D. Gresch, C. Johnson, T. Koretsune *et al.*, Wannier90 as a community code: New features and applications, J. Phys.: Condens. Matter **32**, 165902 (2020).

[54] J. Heyd, G. E. Scuseria, and M. Ernzerhof, Hybrid functionals based on a screened Coulomb potential, J. Chem. Phys. **118**, 8207 (2003).

[55] A. V. Krukau, O. A. Vydrov, A. F. Izmaylov, and G. E. Scuseria, Influence of the exchange screening parameter on the performance of screened hybrid functionals, J. Chem. Phys. **125**, 224106 (2006).

[56] M. J. Wei, W. J. Lu, R. C. Xiao, H. Y. Lv, P. Tong, W. H. Song, and Y. P. Sun, Manipulating charge density wave order in monolayer $1T$-$TiSe_2$ by strain and charge doping: A first-principles investigation, Phys. Rev. B **96**, 165404 (2017).

[57] B. Singh, C.-H. Hsu, W.-F. Tsai, V. M. Pereira, and H. Lin, Stable charge density wave phase in a $1T$-$TiSe_2$ monolayer, Phys. Rev. B **95**, 245136 (2017).

[58] See Supplemental Material at http://link.aps.org/supplemental/10.1103/PhysRevB.108.165421 for Figs. S1–S6 and Table S1.

[59] P. Tsipas, D. Tsoutsou, S. Fragkos, R. Sant, C. Alvarez, H. Okuno, G. Renaud, R. Alcotte, T. Baron, and A. Dimoulas, Massless Dirac fermions in $ZrTe_2$ semimetal grown on InAs(111) by van der Waals epitaxy, ACS Nano **12**, 1696 (2018).

[60] S. L. Dudarev, G. A. Botton, S. Y. Savrasov, C. J. Humphreys, and A. P. Sutton, Electron-energy-loss spectra and the structural stability of nickel oxide: An LSDA+U study, Phys. Rev. B **57**, 1505 (1998).

[61] B. Hildebrand, T. Jaouen, M.-L. Mottas, G. Monney, C. Barreteau, E. Giannini, D. R. Bowler, and P. Aebi, Local real-space view of the achiral $1T$-TiSe$_2$ $2\times2\times2$ charge density wave, Phys. Rev. Lett. **120**, 136404 (2018).

[62] M. Spera, A. Scarfato, Á. Pásztor, E. Giannini, D. R. Bowler, and C. Renner, Insight into the charge density wave gap from contrast inversion in topographic STM images, Phys. Rev. Lett. **125**, 267603 (2020).

[63] M. Tomić, H. O. Jeschke, and R. Valentí, Unfolding of electronic structure through induced representations of space groups: Application to fe-based superconductors, Phys. Rev. B **90**, 195121 (2014).

[64] T. Kaneko, Y. Ohta, and S. Yunoki, Exciton-phonon cooperative mechanism of the triple-q charge-density-wave and antiferro-electric electron polarization in TiSe$_2$, Phys. Rev. B **97**, 155131 (2018).

[65] Through a tight-binding band analysis [64], the conduction bands of monolayer TiSe$_2$ at the three M points of the BZ were found to be characterized by Ti $d_{x'y'}$, $d_{y'z'}$, and $d_{z'x'}$ orbitals in the local coordinate system of the TiSe$_6$ octahedron, respectively. Considering the common band character of semimetallic $1T$ group-IV TMDs, we expect the same physical picture occurs in the sister compounds of monolayer TiTe$_2$ and ZrTe$_2$ studied in the present work.